Available online at www.sciencedirect.com
SCIENCE DIRECT®
International Journal of Heat and Mass Transfer 48 (2005) 1137–1144
International Journal of HEAT and MASS TRANSFER
www.elsevier.com/locate/ijhmt

Melting and dynamic-surface deformation in laser surface heating

Bok-Cheol Sim, Woo-Seung Kim *

Department of Mechanical Engineering, Hanyang University, Sa 1-Dong, Ansan, Kyunggi-Do 425-791, Korea

Received 16 January 2004; received in revised form 31 August 2004
Available online 8 December 2004

Abstract

Axisymmetric thermocapillary convection during laser melting has been investigated numerically. The dynamic free surface, with pinned contact point at the edge of the molten pool, is obtained as a solution of the coupled transport equations. Free surfaces at the steady state are depressed at the center and convex near the edge of the molten pool because fluid flows away from the center. The surface deformations decrease with increasing *Re* at fixed *Ca*, while they increase with increasing *Ca* at fixed *Re*. The width and depth of the pool, temperature and surface deformation increase with increasing *Bf*. At the transient cases, the size of the pool and surface deformation increase monotonically with time. The shape of the free surface is a bowl bump at a low *Re*, while at a high *Re* two kinds of surface shapes occur with time: bowl and Sombrero-shaped bumps.
© 2004 Elsevier Ltd. All rights reserved.

1. Introduction

Lasers are used to weld because of efficiency in heating localized regions and to produce new properties due to rapid heating and cooling rates through laser surface treatment. Laser melting and surface deformation have attracted much attention due to a variety of industrial applications such as welding, fabrication of microstructures and laser zone texturing. Accordingly, many studies have been performed to examine the shape of liquid pool, heat transfer, fluid flow and surface topography in laser-materials interaction. Most studies investigated laser melting problems with non-deformable and flat surfaces. A few included free surface deformations in laser melting problems.

Srinivasan and Basu [1] showed that buoyancy forces in the fluid during laser melting could be neglected. Basu and Date [2], Ravindran et al. [3] and Kim and Sim [4] investigated laser-melting problems with non-deformable flat surfaces in the molten pool.

Baumgart et al. [5], Chen et al. [6] and Willis and Xu [7] investigated experimentally the shape of free surface during pulsed laser-materials interaction. They found several kinds of surface shapes by varying the laser pulse energy. Two-dimensional numerical simulations with deforming surfaces during laser-material interaction were studied by Bennett et al. [8], Iwamoto et al. [9] and Fan et al. [10]. Iwanmoto et al. [9] used a simplified incomplete equation for deforming free surfaces and marker and cell method (MAC), and found that the free surface was a bowl shape. Fan et al. [10] considered electromagnetic, buoyancy, arc drag, and thermocapillary

* Corresponding author. Tel.: +82 31 400 5248; fax: +82 31 418 0153.
E-mail address: wskim@hanyang.ac.kr (W.-S. Kim).

0017-9310/$ - see front matter © 2004 Elsevier Ltd. All rights reserved.
doi:10.1016/j.ijheatmasstransfer.2004.08.032

Nomenclature

Bf	boundary heating factor, $\frac{q'' r_0 C_p}{k_l \lambda}$
Ca	Capillary number, $\frac{\gamma\lambda}{\sigma_0 C_p}$
C_p	specific heat
H	nondimensional enthalpy
k	nondimensional thermal conductivity
Ma	Marangoni number, $Pr \cdot Re$
P	nondimensional pressure
Pr	Prandtl number, $\frac{\nu}{\alpha}$
q''	power density of the beam
r	radial direction
r_{max}	maximum width of the molten pool
r_0	radius of the beam
Re	Reynolds number, $\frac{U_R r_0}{\nu}$
Ste	Stefan number, $\frac{C_p(T_m - T_\infty)}{\lambda}$
t	nondimensional time
T	nondimensional temperature
T_m	melting temperature
U_R	surface tension reference velocity, $\frac{\gamma\lambda}{C_p \mu}$
u	nondimensional radial velocity
V	nondimensional liquid volume
$\mathbf{v}$	nondimensional velocity vector
v	nondimensional axial velocity
z	axial or vertical direction

Greek symbols

λ	latent heat of fusion
ν	kinematic viscosity
μ	dynamic viscosity
α	thermal diffusivity
γ	$-\partial\sigma/\partial T$
σ	surface tension
ρ	density

Subscripts

l	liquid
s	solid
0	reference state
∞	ambient

Superscript

*	dimensional quantity

forces during gas tungsten arc welding, and solved dynamic free surfaces with only surface pressure distribution. Free surface should be determined by both surface pressure and normal viscous stresses.

In the present work we report on thermocapillary convection in laser melting problems with deformable interfaces by two-dimensional numerical simulations. The shape of the free surface is unknown and is calculated as the part of the complete solution. Numerical results with non-deformable flat surfaces are compared with those from other studies. The influence of surface deformation on convection is investigated.

2. Mathematical model

The physical system considered is shown in Fig. 1. A stationary, continuous, axisymmetric laser beam of radius r_0 with a uniform heat flux irradiates the surface. The beam radii of 1 mm and 0.5 mm are used to compare with, respectively, numerical [3] and experimental [11] results. The uniform heat flux is reasonable because the radius of the laser beam is so small. All of the incident energy is assumed to be absorbed into the material. The top surface outside the beam is adiabatic, and the bottom and side walls have constant temperatures, $T_\infty = 300$ K. Melting occurs beneath the beam, and the flow in the molten pool is a surface tension driven flow due to a temperature gradient along a free surface which is thermocapillary convection. Surface tension is assumed a linear function of temperature,

$$\sigma = \sigma_0 - \gamma(T^* - T_0). \quad (1)$$

With negligible body forces, the nondimensional governing equations are:

$$\nabla \cdot \mathbf{v} = 0, \quad (2)$$

$$\frac{1}{Ma}\frac{\partial \mathbf{v}}{\partial t} + \nabla \cdot (\mathbf{v}\mathbf{v}) = -\nabla P + \frac{1}{Re}\nabla^2 \mathbf{v}, \quad (3)$$

$$\frac{\partial H}{\partial t} + Ma\nabla \cdot (\mathbf{v}H) = \nabla \cdot (k\nabla T). \quad (4)$$

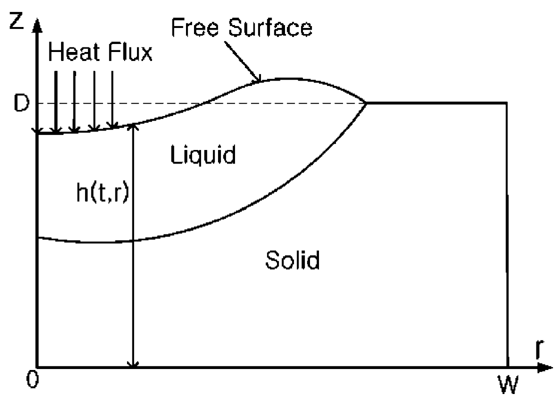

Fig. 1. Physical system.

The boundary conditions considered are:

$$\frac{\partial T}{\partial r} = u = \frac{\partial v}{\partial r} = 0, \quad \text{at } r = 0, \tag{5}$$

$$T = -Ste, \quad u = v = 0, \quad \text{at } r = W, \tag{6}$$

$$T = -Ste, \quad u = v = 0, \quad \text{at } z = 0. \tag{7}$$

The non-dimensionalized position of the free surface is described by a function $h(t, r)$. Thermal, kinematic and tangential and normal stress balance boundary conditions at the interface are

$$\frac{1}{N}\left(-h'\frac{\partial T}{\partial r} + \frac{\partial T}{\partial z}\right) = Bf, \tag{8}$$

$$v = \frac{1}{Ma}\frac{\partial h}{\partial t} + h'u, \tag{9}$$

$$(1 - h'^2)\left(\frac{\partial u}{\partial z} + \frac{\partial v}{\partial r}\right) + 2h'\left(\frac{\partial v}{\partial z} - \frac{\partial u}{\partial r}\right) = -N\left(\frac{\partial T}{\partial r} + h'\frac{\partial T}{\partial z}\right), \tag{10}$$

$$-Re \cdot P + \frac{2}{N^2}\left[\frac{\partial v}{\partial z} + h'^2\frac{\partial u}{\partial r} - h'\left(\frac{\partial v}{\partial r} + \frac{\partial u}{\partial z}\right)\right] = \frac{1 - CaT}{CaN}\left(\frac{h''}{N^2} + \frac{h'}{r}\right), \tag{11}$$

where $N = (1 + h'^2)^{1/2}$, $h' = \frac{\partial h}{\partial r}$, and $Bf = 0$ at $r > 1$. Ca provides a measure of surface deflection in response to thermocapillary-induced stresses. If $Ca = 0$ (large surface tension), the dynamic surface deformations can be neglected and the free surface is non-deformable. Free-surface curvature is determined by both surface pressure and normal viscous stresses as shown in Eq. (11). The nondimensional variables are as follows:

$$t = \frac{t^*\alpha}{r_0^2}, \quad r = \frac{r^*}{r_0}, \quad \mathbf{v} = \frac{\mathbf{v}^*}{U_R}$$
$$P = \frac{P^*}{\rho U_R^2}, \quad T = \frac{C_p(T^* - T_m)}{\lambda}, \quad k = \frac{k^*}{k_l}$$

The initial and boundary conditions for Eq. (11) are:

$$h(t = 0, r) = D, \quad h'(t, r = 0) = 0, \quad h(t, r = r_1) = D, \tag{12}$$

where $r_1 = \frac{r_{max}}{r_0}$. The liquid volume must satisfy the mass conservation, and its changed total volume should be zero:

$$V = \int_0^{r_1}(h - D)r\,\mathrm{d}r = 0, \tag{13}$$

where V is the non-dimensional liquid volume.

3. Numerical aspects

In order to solve the problem with a deformable surface, the equations are transformed from the physical domain (t, r, z) into a rectangular computational domain(t, ξ, η).

$$\xi = r \tag{14}$$

$$\eta = \frac{zD}{h(t, r)} \tag{15}$$

The transformed governing equations are

$$\frac{1}{\xi}\frac{\partial \xi u}{\partial \xi} - \eta\frac{h'}{h}\frac{\partial u}{\partial \eta} + \frac{D}{h}\frac{\partial v}{\partial \eta} = 0, \tag{16}$$

$$\frac{1}{Ma}\left[\frac{\partial u}{\partial t} - \frac{\eta}{h}\frac{\partial h}{\partial t}\frac{\partial u}{\partial \eta}\right] + \frac{1}{\xi}\frac{\partial \xi u^2}{\partial \xi} - \eta\frac{h'}{h}\frac{\partial u^2}{\partial \eta} + \frac{D}{h}\frac{\partial uv}{\partial \eta} = -\frac{\partial P}{\partial \xi} + \eta\frac{h'}{h}\frac{\partial P}{\partial \eta} + \frac{1}{Re}\left[\nabla^2 u - \frac{u}{\xi^2}\right], \tag{17}$$

$$\frac{1}{Ma}\left[\frac{\partial v}{\partial t} - \frac{\eta}{h}\frac{\partial h}{\partial t}\frac{\partial v}{\partial \eta}\right] + \frac{1}{\xi}\frac{\partial \xi uv}{\partial \xi} - \eta\frac{h'}{h}\frac{\partial uv}{\partial \eta} + \frac{D}{h}\frac{\partial v^2}{\partial \eta} = -\frac{D}{h}\frac{\partial P}{\partial \eta} + \frac{1}{Re}\nabla^2 v, \tag{18}$$

$$\frac{\partial T}{\partial t} - \frac{\eta}{h}\frac{\partial h}{\partial t}\frac{\partial T}{\partial \eta} + Ma\left[\frac{1}{\xi}\frac{\partial \xi uT}{\partial \xi} - \eta\frac{h'}{h}\frac{\partial uT}{\partial \eta} + \frac{D}{h}\frac{\partial vT}{\partial \eta}\right] = \frac{1}{\xi}\frac{\partial}{\partial \xi}\left(k\xi\frac{\partial T}{\partial \xi}\right) - \frac{\eta h'}{h}\left[\frac{\partial}{\partial \eta}\left(k\frac{\partial T}{\partial \xi}\right) + \frac{\partial}{\partial \xi}\left(k\frac{\partial T}{\partial \eta}\right)\right] + \left[2\left(\frac{h'}{h}\right)^2 - \frac{h''}{h} - \frac{h'}{h\xi}\right]\eta k\frac{\partial T}{\partial \eta} + \left[\left(\frac{h'\eta}{h}\right)^2 + \frac{D^2}{h^2}\right]\frac{\partial}{\partial \eta}\left(k\frac{\partial T}{\partial \eta}\right) - \frac{\partial f}{\partial t}, \tag{19}$$

$$\nabla^2 = \frac{1}{\xi}\frac{\partial}{\partial \xi}\left(\xi\frac{\partial}{\partial \xi}\right) - \frac{2\eta h'}{h}\frac{\partial^2}{\partial \eta \partial \xi} + \left[2\left(\frac{h'}{h}\right)^2 - \frac{h''}{h} - \frac{h'}{h\xi}\right]\eta\frac{\partial}{\partial \eta} + \left[\left(\frac{h'\eta}{h}\right)^2 + \frac{D^2}{h^2}\right]\frac{\partial^2}{\partial \eta^2}, \tag{20}$$

where f is the local liquid fraction. For a liquid control volume without a mushy zone, $f = 1$ while for a solid $f = 0$. The latent heat of fusion is accounted by the source term [12], $\frac{\partial f}{\partial t}$, in the energy equation, Eq. (19).

The transformed boundary conditions become

$$\text{At } \xi = 0, \quad \frac{\partial T}{\partial \xi} = u = \frac{\partial v}{\partial \xi} = 0, \tag{21}$$

$$\text{At } \xi = W, \quad T = -Ste, \quad u = v = 0, \tag{22}$$

$$\text{At } \eta = 0, T = -Ste, \quad u = v = 0. \tag{23}$$

At the interface ($\eta = D$),

$$\frac{D(1+h'^2)}{h}\frac{\partial T}{\partial \eta} - h'\frac{\partial T}{\partial \xi} = NBf, \tag{24}$$

$$v = \frac{1}{Ma}\frac{\partial h}{\partial t} + h'u, \tag{25}$$

$$D\left(\frac{1+h'^2}{h}\right)\frac{\partial u}{\partial \eta} - 2h'\frac{\partial u}{\partial \xi} + D\left(\frac{h'+h'^3}{h}\right)\frac{\partial v}{\partial \eta} + (1-h'^2)\frac{\partial v}{\partial \xi} = -N\frac{\partial T}{\partial \xi}, \tag{26}$$

$$-Re\cdot P + \frac{2D}{h}\left(\frac{\partial v}{\partial \eta} - h'\frac{\partial u}{\partial \eta}\right) + \frac{2h'}{N^2}\left(h'\frac{\partial u}{\partial \xi} - \frac{\partial v}{\partial \xi}\right) = \frac{1-CaT}{CaN}\left(\frac{h''}{N^2} + \frac{h'}{\xi}\right), \tag{27}$$

as in Eq. (11), P contains a free integration constant, $c(t)$. $h(t, r)$ and $c(t)$ are determined by Eqs. (27), (12) and (13). A shooting method is used to find $c(t)$ at each time.

The free-surface shape, $h(t,r)$, is unknown and should be obtained as a solution of the coupled governing equations along with the surface force balance. The transformed governing Eqs. (16)–(19) and boundary conditions, Eqs. (21)–(27), are solved by a finite volume method employing a SIMPLER algorithm. Nonuniform grids are constructed with finer meshes in the regions under the free surface and near the center. All computations are started with $h = D$, $\mathbf{v} = 0$ and $T = -Ste$. A brief summary of the computational procedure is as follows [13,14]:

1. Start with initial conditions for T, $\mathbf{v}$, and h.
2. Solve the conduction equation to find T until melting starts (This step is skipped if a molten pool exists).
3. The rectangular computational domain is generated numerically.
4. Solve the transformed governing equations, Eqs. (16)–(19), to find T and $\mathbf{v}$ with the transformed boundary conditions, Eqs. (21)–(26).
5. Calculate h and c with the normal stress balance and liquid volume equations, Eqs. (27), (12) and (13).
6. Steps (3)–(5) are repeated at each time step until all conditions for T, $\mathbf{v}$, and h are satisfied with the desired accuracy.
7. Return to step (1) for the next time.

Convergence criterion for a steady state is $|s^{n+1} - s^n|/|s^{n+1}| < 10^{-3}$, where s is any variable(u, v, T, h) at all points and n is time iteration level. In order to examine grid dependence, free surface temperature and velocity distributions are computed with various grids in Fig. 2. The errors of the maximum temperatures and velocities with two different grid points are less than 5% in Fig. 2, and the grid-independence is achieved with $41(r)\times 41(z)$ grid points. A mesh of $41(r)\times 41(z)$ grid points with nonuniform grids is used for all computations.

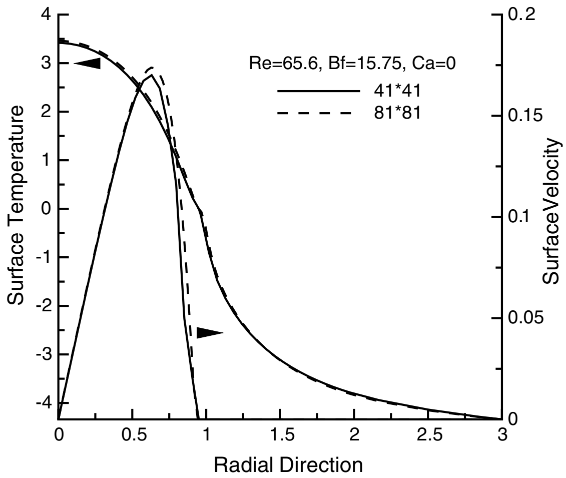

Fig. 2. Surface temperature and velocity distributions with various grids (Re = 65.6, Bf = 15.75 and Ca = 0). Grid independence almost achieved.

4. Results and discussion

Property values of steel and nondimensional parameters for numerical simulations are shown in Table 1. The numerical code is based on [15,16], and the the numerical results in our previous work [15] were in good quantitative agreement with experiments, which have no phase-change. In order to validate the numerical code

Table 1
Property values of steel [3]

Variable	Value	Nondimensional value
ρ	7200 (kg/m^3)	
k_s	31.39 (W/m K)	
λ	2.47×10^5 (J/kg)	
T_∞	300 (K)	Ste = 4.338
r_0	1 (mm)	
T_m	1723 (K)	
C_p	753 (J/kg K)	
k_l	15.48 (W/m K)	
μ	0.006 (N s/m^2)	Pr = 0.292
q	6×10^7 (W/m^2)	Bf = 11.82
	8×10^7 (W/m^2)	Bf = 15.75
	1.2×10^8 (W/m^2)	Bf = 23.63
γ	-10^{-6} (N/m K)	Re = 65.6
	-10^{-5} (N/m K)	Re = 656
	-10^{-4} (N/m K)	Re = 6560

Table 2
Comparison of molten pool shape and maximum temperature

Re	Present results			Ravindran et al. [3]		
	Width	Depth	T_{max}	Width	Depth	T_{max}
65.6	0.95	0.26	3.418	0.91	0.28	3.649
6560	0.97	0.19	2.217	0.97	0.18	2.155
Bf				Experiments [11]		
3.456	0.845	0.31		0.82	0.35	
4.541	0.99	0.425		1.00	0.46	
6.203	1.151	1.016		1.2	1.00	

Bf = 15.75 for the numerical results [3], and r_0 = 0.5 mm, *Ma* = 1851, *Pr* = 0.009, *Re* = 201960 and *Ste* = 1.2117 for the experiment [11].

with phase-change, the computed pool shape and maximum temperature are compared with numerical [3] and experimental [11] results in Table 2, where the experiment is for Al–4.5%Cu. Ravindran et al. [3] solved the energy equation with the apparent capacity method. The present results are in good agreement with the numerical [3] and experimental [11] results.

4.1. Steady thermocapillary convection

Fig. 3 shows free surfaces at steady state with *Ca* = 0.01, *Bf* = 15.75 and various *Re*. The corresponding surface temperature and velocity distributions are shown in Fig. 4. The free surface is depressed at the center and convex near the edge of the molten pool because fluid flows away from the center. As *Re* increases, the surface temperature gradient and hence the surface velocity decreases as shown in Fig. 4. The maximum temperature and velocity increase as *Re* decreases. The increased velocities induce larger surface deformations

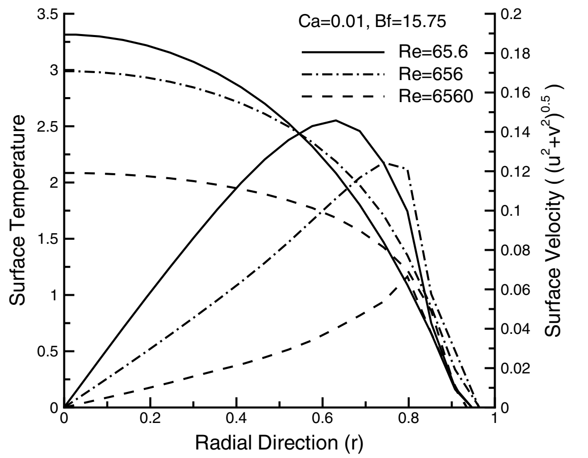

Fig. 4. Surface temperature and velocity distributions associated with Fig. 3. Maximum temperature and velocity increase with decreasing *Re*.

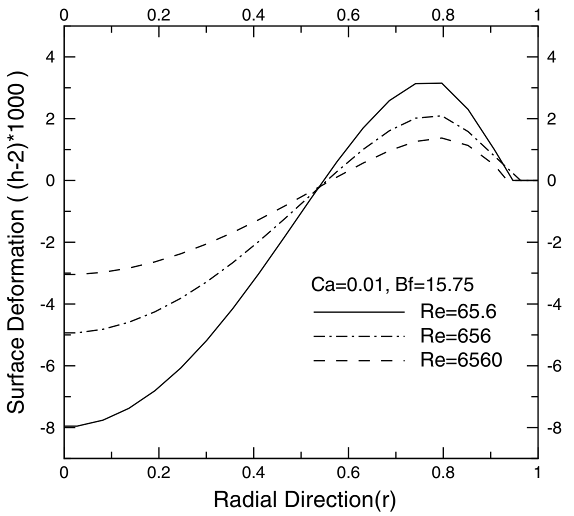

Fig. 3. Free surface deformations with *Ca* = 0.01, *Bf* = 15.75 and various *Re*. Crater depth and rim height increase with decreasing *Re* at a fixed *Ca*.

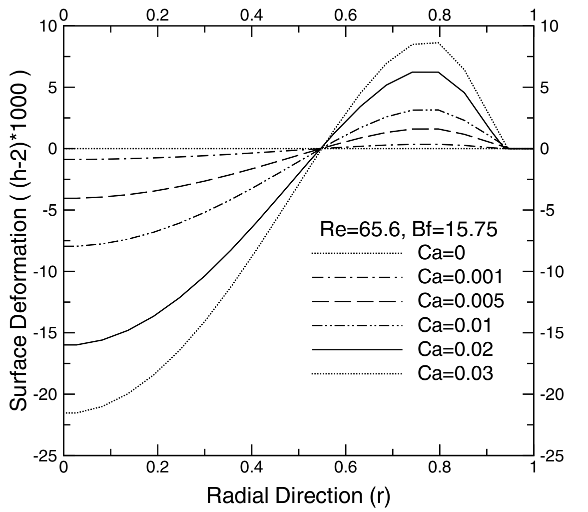

Fig. 5. Free surface deformations with *Re* = 65.6, *Bf* = 15.75 and various *Ca*. As $Ca \rightarrow 0$, surface deformations can be neglected.

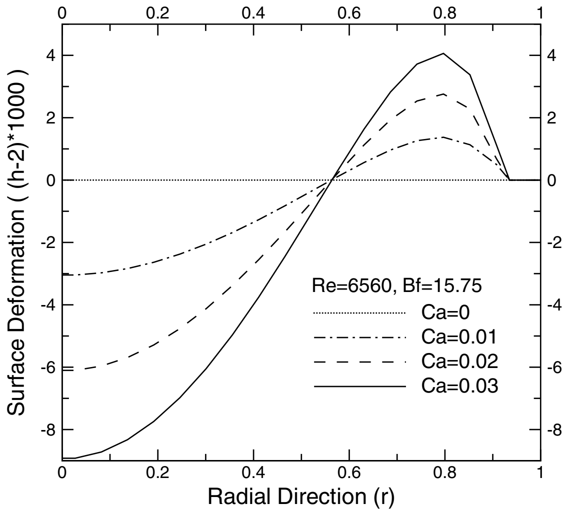

Fig. 6. Similar to Fig. 5 but with $Re = 6560$. Surface deformations increase with increasing Ca at a fixed Re.

Table 3
Molten pool shape and maximum temperature with $Bf = 15.75$

Re	Ca	Width	Depth	T_{max}
65.6	0	0.95	0.26	3.418
	0.01	0.95	0.26	3.314
	0.02	0.94	0.25	3.125
	0.03	0.95	0.25	3.117
6560	0	0.97	0.19	2.217
	0.01	0.94	0.17	2.085
	0.02	0.94	0.18	2.073
	0.03	0.94	0.18	2.104

at a fixed Ca. Thus, the surface deformations increase with decreasing Re at fixed Ca.

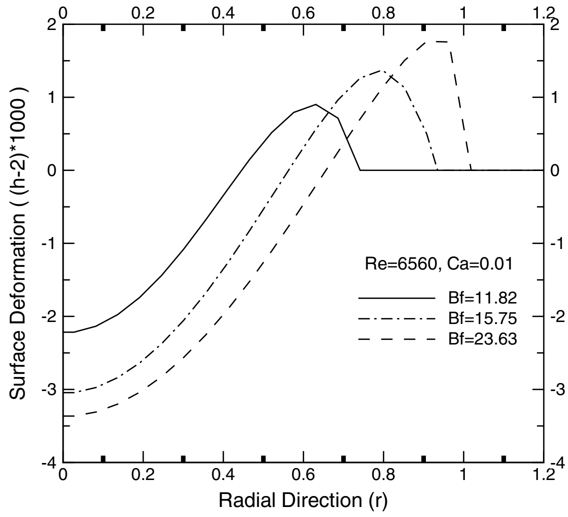

Fig. 7. Effect of Bf on surface deformation with $Re = 6560$ and $Ca = 0.01$. Surface deformation becomes larger with increasing Bf.

Figs. 5 and 6 show the variations of the free surface with Ca at fixed $Re = 65.6$ and 6560, respectively. As $Ca \rightarrow 0$, surface tension increases and the dynamic surface deformations can be neglected. The shape of the free surface, number of ripples, and reflection point do not change with Ca at a fixed Re, while the surface deformations, the magnitude of depressions and elevations, increase with increasing Ca due to small surface tension. Surface deformation is $O(10^{-3})$. Its maximum value is 2.15×10^{-2}, about 8.6% of the molten depth, with $Re = 65.6$ and $Ca = 0.03$. The effect of Ca on maximum temperature and shape of the molten pool is shown in Table 3. They are almost insensitive to variations in Ca at fixed Re. Ca at fixed Re has little effect

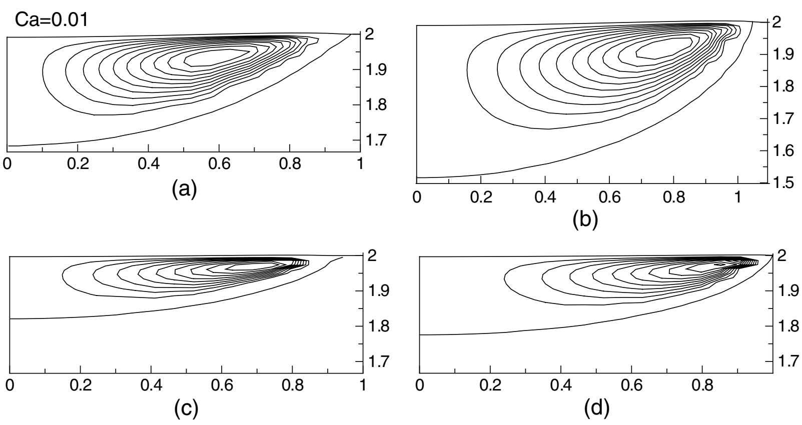

Fig. 8. Streamlines with $Ca = 0.01$: (a) $Re = 65.6$ and $Bf = 15.75$, (b) $Re = 65.6$ and $Bf = 23.63$, (c) $Re = 6560$ and $Bf = 15.75$, and (d) $Re = 6560$ and $Bf = 23.63$. Depth of the molten pool decreases with increasing Re at fixed Bf, while the depth and width increase with increasing Bf at fixed Re.

on the convection, while *Re* substantially influences the convection at fixed *Ca*.

Fig. 7 shows effect of *Bf* on the free surfaces with $Re = 6560$ and $Ca = 0.01$. The streamlines in the molten pool are shown in Fig. 8 with $Ca = 0.01$. As expected, the width and depth of the molten pool, temperature and surface deformation increase with increasing *Bf* at fixed *Re*. While the depth of the pool decreases with increasing *Re* at fixed *Bf*, the width is almost independent of *Re*. As *Bf* increases at fixed *Re*, the center of the convection cell moves closer to the free surface and the melt interface due to stronger convection. The flow fields show a large toroidal, single-cell flow, which is a typical axisymmetric thermocapillary convection. Therefore, detailed discussions are omitted here and can be found in other studies with a non-deformable flat surface [2–4].

4.2. Transient thermocapillary convection

Ca is in the range 0.000169–0.0169 with $-10^{-6} \leqslant \gamma \leqslant -10^{-4}$ and $\sigma_0 = 1.943\,\mathrm{N/m}$ [10]. Figs. 9 and 10 show transient surface deformations with $Ca = 0.02$ and $Bf = 15.75$ at fixed $Re = 65.6$ and 6560, respectively. The width of the pool and surface deformations at a low *Re* increase monotonically with time as shown in Fig. 9. With $Re = 6560$ and $Ca = 0.02$, the surface deformations increase until $t = 2$, and then decrease slightly with time as shown in Fig. 10. Two kinds of the surface shapes occur with time: bowl and Sombrero-shaped bumps. These two shapes are in good qualitative agreement with transient results from experiments [5,6], where the experiments are for glass without latent heat of fusion. Several shapes of the free surfaces can be found in [6–8].

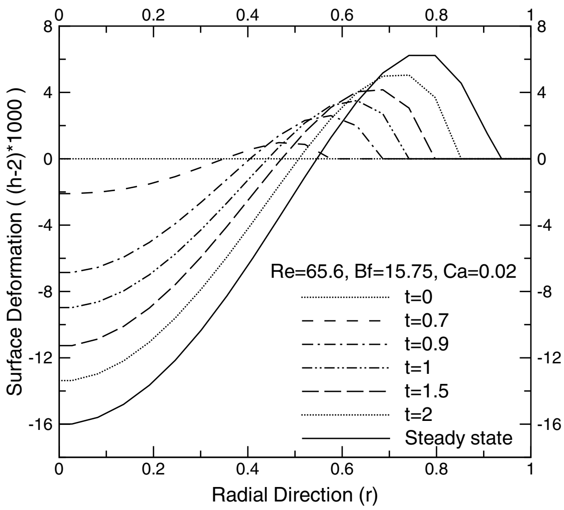

Fig. 9. Transient surface deformations with $Re = 65.6$, $Ca = 0.02$ and $Bf = 15.75$. Molten pool and surface deformation increase monotonically with time.

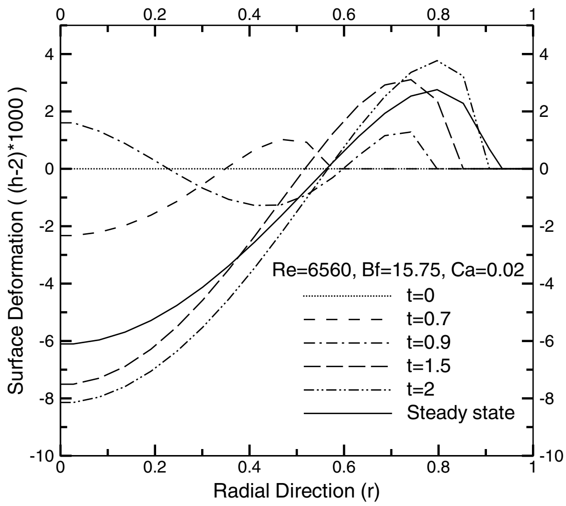

Fig. 10. Similar to Fig. 9 but with $Re = 6560$. Two kinds of surface shapes occur with time: bowl and Sombrero-shaped bumps.

Fig. 11 shows transient flow patterns corresponding to Fig. 10. The shape of the molten pool changes rapidly during the earlier time, and then the change rate decreases. The size, width and depth, of the pool increases

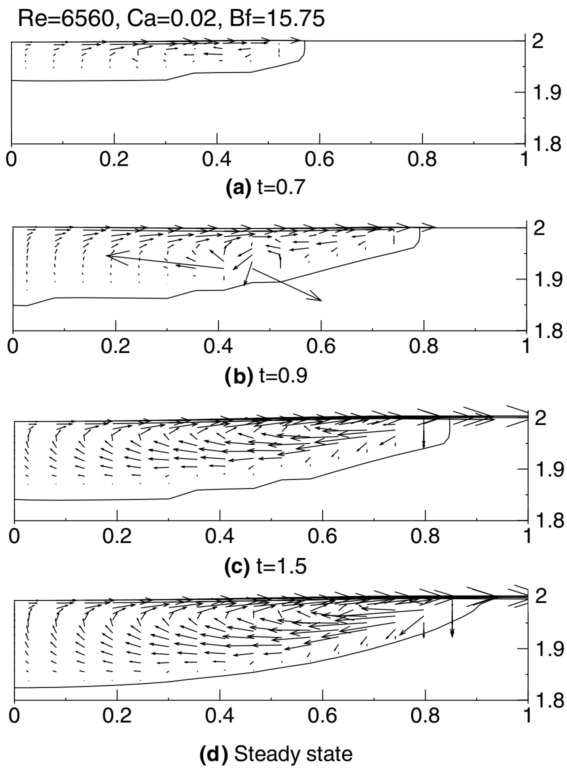

Fig. 11. Transient flow pattern corresponding to Fig. 10.

with time. The noticeable change in flow fields occurs at $t = 0.9$ as shown in Fig. 11(b). At the transition ($t = 0.9$), the surface shape changes very much as shown in Fig. 10 and hence the flow is unstable in Fig. 11(b), vice versa.

It is well known that steady thermocapillary flow undergoes a transition to oscillatory time-dependent, three-dimensional flow [17–20]. However, flow instabilities are not investigated here due to their three-dimensional nature. The instabilities on thermocapillary convection in open cylinders with a uniform heat flux can be found in [15].

5. Conclusions

Axisymmetric thermocapillary convection during laser melting has been investigated numerically to analyze molten pools and surface deformations. The dynamic free surface, with pinned contact point at the edge of the molten pool, is obtained as a solution of the coupled transport equations and boundary conditions.

Free surfaces at steady state are depressed at the center and convex near the edge of the molten pool because fluid flows away from the center. The surface deformations decrease with increasing Re at fixed Ca, while they increase with increasing Ca at fixed Re. The surface deformation is $O(10^{-3})$. Its maximum value is 2.15×10^{-2}, about 8.6% of the molten depth, with $Re = 65.6$ and $Ca = 0.03$. The width and depth of the pool, temperature and surface deformation increase with increasing Bf.

In the case of transition, the size of the pool and surface deformation increase monotonically with time. The shape of the free surface is a bowl bump at a low Re, while at a high Re two kinds of surface shapes occur with time: bowl and Sombrero-shaped bumps.

Acknowledgment

This work was supported by the Brain Korea 21 Project in 2003. We gratefully acknowledge the support of BK 21.

References

[1] J. Srinivasan, B. Basu, A numerical study of thermocapillary flow in a rectangular cavity during laser melting, Int. J. Heat Mass Transfer 24 (1986) 563–573.
[2] B. Basu, A.W. Date, Numerical study of steady state and transient laser melting problems-I. Characteristics of flow field and heat transfer, Int. J. Heat Mass Transfer 33 (6) (1990) 1149–1163.
[3] K. Ravindran, J. Srinivasan, A.G. Marathe, Finite element study of the role of convection in laser surface melting, Numer. Heat Transfer Part A 26 (1994) 601–618.
[4] W.-S. Kim, B.-C. Sim, Study of thermal behavior and fluid flow during laser surface heating of alloys, Numer. Heat Transfer Part A 31 (1997) 703–723.
[5] P. Baumgart, D.J. Krajnovich, T.A. Nguyen, A.C. Tam, A new laser texturing technique for high performance magnetic disk drives, IEEE Trans. Magnet. 31 (6) (1995) 2946–2951.
[6] S.C. Chen, D.G. Cahill, C.P. Grigoropoulos, Melting and surface deformation in pulsed laser surface micromodification of Ni-P disks, J. Heat Transfer 122 (2000) 107–112.
[7] D.A. Willis, X. Xu, Transport phenomena and droplet formation during pulsed laser interaction with thin films, J. Heat Transfer 122 (2000) 763–770.
[8] T.D. Bennett, D.J. Krajnovich, C.P. Grigoropoulos, P. Baumgart, A.C. Tam, Marangoni mechanism in pulsed laser texturing of magnetic disk substrates, J. Heat Transfer 119 (1997) 589–596.
[9] M. Iwamoto, M. Ye, C.P. Grigoropoulos, R. Greif, Numerical analysis of pulsed laser heating for the deformation of metals, Numer. Heat Transfer Part A 34 (1998) 791–804.
[10] H.G. Fan, H.L. Tsai, S.J. Na, Heat transfer and fluid flow in a partially or fully penetrated weld pool in gas tungsten arc welding, Int. J. Heat Mass Transfer 44 (2001) 417–428.
[11] J. Sekhar, Rapid solidification of alloy substrates by lasers and electron beams: heat flow modeling and solidification morphology, Ph.D. thesis, University of Illinois, Urbana-Champaign, 1982.
[12] C.R. Swaminathan, V.R. Voller, On the enthalpy method, Int. J. Numer. Meth. Heat Fluid Flow 3 (1993) 233–244.
[13] B.-C. Sim, W.-S. Kim, A. Zebib, Axisymmetric thermocapillary convection in open cylindrical annuli with deforming interfaces, Int. J. Heat Mass Transfer 47 (2004) 5365–5373.
[14] B.-C. Sim, W.-S. Kim, A. Zebib, Dynamic free-surface deformations in axisymmetric liquid bridges, Adv. Space Res. 34 (2004) 1627–1634.
[15] B.-C. Sim, A. Zebib, Thermocapillary convection with undeformable curved surfaces in open cylinders, Int. J. Heat Mass Transfer 45 (25) (2002) 4983–4994.
[16] B.-C. Sim, A. Zebib, Thermocapillary convection in cylindrical liquid bridges and annuli, C. R. Mecanique 332 (2004) 473–486.
[17] B.-C. Sim, A. Zebib, Thermocapillary convection with undeformable curved surfaces in liquid bridges, J. Thermophys. Heat Transfer 16 (2002) 553–561.
[18] B.-C. Sim, A. Zebib, Effect of surface heat loss and rotation on transition to oscillatory thermocapillary convection, Phys. Fluids 14 (2002) 225–231.
[19] D. Schwabe, A. Zebib, B.-C. Sim, Oscillatory thermocapillary convection in open cylindrical annuli. Part 1. Experiments under microgravity, J. Fluid Mech. 491 (2003) 239–258.
[20] B.-C. Sim, A. Zebib, D. Schwabe, Oscillatory thermocapillary convection in open cylindrical annuli. Part 2. Simulations, J. Fluid Mech. 491 (2003) 259–274.